

Cite this: *Dalton Trans.*, 2022, **51**, 2517

## Towards the design of contrast-enhanced agents: systematic Ga<sup>3+</sup> doping on magnetite nanoparticles†

Itziar Galarreta-Rodriguez,<sup>a</sup> Lourdes Marcano,<sup>b,c</sup> Idoia Castellanos-Rubio,<sup>b</sup> Izaskun Gil de Muro,<sup>a</sup> Isabel García,<sup>d,e</sup> Luca Olivi,<sup>f</sup> M. L. Fernández-Gubieda,<sup>b</sup> Ainara Castellanos-Rubio,<sup>g</sup> Luis Lezama,<sup>a</sup> Idoia Ruiz de Larramendi<sup>g</sup> and Maite Insausti<sup>g</sup> \*<sup>a,h</sup>

The main objective of the preparation of the Fe<sub>3-x</sub>Ga<sub>x</sub>O<sub>4</sub> (0.14 ≤ x ≤ 1.35) system was to further the knowledge of the magnetic response of Ga<sup>3+</sup>-doped magnetite for application as MRI contrast agents. With this purpose, monodisperse nanoparticles between 7 and 10 nm with different amounts of gallium were prepared from an optimized protocol based on thermal decomposition of metallo-organic precursors. Thorough characterization of the sample was conducted in order to understand the influence of gallium doping on the structural, morphological and magnetic properties of the Fe<sub>3-x</sub>Ga<sub>x</sub>O<sub>4</sub> system. X-ray diffraction and X-ray absorption near-edge structure measurements have proved the progressive incorporation of Ga in the spinel structure, with different occupations in both tetrahedral and octahedral sites. Magnetization measurements as a function of field temperature have shown a clear dependence of magnetic saturation on the gallium content, reaching an M<sub>s</sub> value of 110 Am<sup>2</sup> kg<sup>-1</sup> at 5 K for x = 0.14 (significantly higher than bulk magnetite) and considerably decreasing for amounts above x = 0.57 of gallium. For this reason, nanoparticles with moderate Ga quantities were water-transferred by coating them with the amphiphilic polymer PMAO to further analyse their biomedical potential. Cytotoxicity assays have demonstrated that Fe<sub>3-x</sub>Ga<sub>x</sub>O<sub>4</sub>@PMAO formulations with x ≤ 0.57, which are the ones with better magnetic response, are not toxic for cells. Finally, the effect of gallium doping on relaxivities has been analysed by measuring longitudinal (T<sub>1</sub><sup>-1</sup>) and transverse (T<sub>2</sub><sup>-1</sup>) proton relaxation rates at 1.4 T revealing that nanoparticles with x = 0.14 Ga<sup>3+</sup> content present remarkable T<sub>2</sub> contrast and the nanoparticles with x = 0.26 have great potential to act as dual T<sub>1</sub>-T<sub>2</sub> contrast agents.

Received 7th September 2021,  
Accepted 20th December 2021

DOI: 10.1039/d1dt03029a

rsc.li/dalton

<sup>a</sup>Dpto. Química Orgánica e Inorgánica, Facultad de Ciencia y Tecnología, UPV/EHU, Sarriena s/n, 48940 Leioa, Spain. E-mail: maite.insausti@ehu.eus

<sup>b</sup>Dpto. Electricidad y Electrónica, Facultad de Ciencia y Tecnología, UPV/EHU, Sarriena s/n, 48940 Leioa, Spain

<sup>c</sup>Helmholtz-Zentrum Berlin für Materialien und Energie, Albert-Einstein-Straße 15, 12489 Berlin, Germany

<sup>d</sup>CIC biomAGUNE, Basque Research and Technology Alliance (BRTA), Paseo de Miramon 182, 20014 Donostia San Sebastián, Spain

<sup>e</sup>Centro de Investigación Biomédica en Red, Biomateriales, Bioingeniería y Nanomedicina (CIBER-BBN), Spain

<sup>f</sup>Elettra Sincrotron Trieste, 34149 Basovizza, Italy

<sup>g</sup>Dpto. Genética, Antropología Física y Fisiología Animal, Facultad de Medicina, UPV/EHU, Leioa, Spain

<sup>h</sup>BCMaterials, Basque Center for Materials, Applications and Nanostructures, UPV/EHU Science Park, 48940 Leioa, Spain

†Electronic supplementary information (ESI) available: thermogravimetry, Rietveld refinements, fit M(H), ZFC-FC, the Scherrer calculation, DLS measurements, etc. See DOI: 10.1039/d1dt03029a

## 1. Introduction

Current research in magnetic nanoparticles (MNPs) is aimed at applying them as T<sub>1</sub> and T<sub>2</sub> contrast enhancement magnetic resonance imaging (MRI) agents, as drug carriers, in the generation of heat by magnetic hyperthermia or in magnetic manipulation/cell-targeting in the biomedical field.<sup>1-4</sup> Fe<sub>3</sub>O<sub>4</sub> nanoparticles are the most widely used material for these applications thanks to their biocompatibility, stability and versatility for modulating magnetic properties by tuning their shape and size or by doping with strategic cations.<sup>5,6</sup> In the last few years, most of the applications of magnetite NPs have focused on the development of multimodal platforms for therapeutic use, for being applied in therapies like magnetic hyperthermia and in the detection of diseases.<sup>7,8</sup>

For efficient magnetic response, homogeneous magnetite NPs with high magnetization are required as also NPs with no remanence to prevent agglomeration.<sup>9</sup> This magnetic behaviour is highly suitable for applications such as T<sub>1</sub> and T<sub>2</sub> con-

trast agents in MRI, mainly  $T_2$  agents, as the innate high magnetic moment of the usually not very small NPs reduces the  $T_1$  contrast capability.<sup>10,11</sup> Doping magnetite with different ions such as Zn(II), Co(II) or Mn(II) has been employed to reduce the amount of Fe(II) ions on the surface and to enhance  $T_1$  relaxivity.<sup>12,13</sup> In the case of dark contrast, the enhancement of  $T_2$  relaxivity has been exploited not only by the strategy of doping but also by controlling morphologies and compositions.<sup>14–17</sup>

Although MRI provides anatomical details with high spatial resolution, in the case of exploring cancer staging, nuclear imaging techniques such as positron emission tomography (PET) or single-photon emission computed tomography (SPECT) are also applied due to high spatial resolution. In this way, the incorporation of  $^{68}\text{Ga}$  in magnetite allows the development of multimodal nanosystems for PET/MRI imaging.<sup>18–20</sup> These kinds of systems have also been proved as magnetomotive ultrasound imaging (MMUS), which detect the movement of the tissue around the NPs under a time-varying magnetic field.<sup>21</sup>

In this sense, gallium ferrites have aroused great interest not only due to the possibility of their use in diagnosis as contrast nanomaterials in MRI or as radiopharmaceuticals but also in medical therapies such as magnetic hyperthermia.<sup>22,23</sup> It is to be noted that despite the traditional applications of gallium-doped ferrites for their magnetoelectrical properties, gallium presents many biological effects in the treatment of bone metastases, Paget's disease, postmenopausal osteoporosis or in some lymphomas.<sup>24,25</sup> All this potentiality in biomedicine has lavished the preparation and characterization of gallium ferrites with different compositions with the aim of tailoring their properties.

Nevertheless, the distribution of  $\text{Ga}^{3+}$  ions in tetrahedral (A) and octahedral (B) positions of the inverse spinel structure of  $\text{Fe}_3\text{O}_4$  is a non-trivial issue. Although the reduced  $\text{Ga}^{3+}$  ion radius would suggest a preference for A sites, the synthesis conditions and the different trends of nanoparticles comparing with bulk material, make it difficult to predict a specific behaviour.<sup>26,27,28</sup> Considering that  $\text{FeGa}_2\text{O}_4$  has emerged as the most promising material in the family of gallium ferrites, most of the research has been focused on the preparation of  $\text{Fe}^{3+}$  substituted  $\text{Fe}_{1+x}\text{Ga}_{2-x}\text{O}_4$  samples. J. Ghose *et al.* revealed that  $\text{Fe}^{3+}$  ions replace  $\text{Ga}^{3+}$  ions with  $\text{Fe}^{2+}$  ion displacement to octahedral positions until  $x = 0.6$  when  $\text{Fe}^{3+}$  ions probably occupy the octahedral positions without displacing  $\text{Fe}^{2+}$  ions to the octahedral positions.<sup>29</sup> This distribution handicaps A–B interactions, which affects the magnetic response of the material. Additionally, it is to be noted that depending on the precursors employed in the synthesis or the annealing conditions  $\text{FeGaO}_3$  can appear as a secondary phase, altering the trend of occupation and the magnetic properties.<sup>30</sup>

With the aim of broadening the knowledge on the structural and magnetic behaviour of gallium ferrites, six different samples with the composition  $\text{Fe}_{3-x}\text{Ga}_x\text{O}_4$  ( $0.14 < x < 1.35$ ) were prepared. All of them were synthesised by the thermal decomposition method using the same heating-rate. To make

them hydrophilic and biocompatible they were functionalized with the polymer poly(maleic anhydride-*alt*-1-octadecene) (PMAO). The structural characterization of synthesised materials was carried out using X-ray diffraction (XRD) and X-ray absorption near edge structure (XANES). The latter, which is sensitive to local structure, provides valuable information about the oxidation-state and site symmetry of metallic cations. The lack of information at both Ga and Fe edges in the literature regarding gallium ferrites makes this study an indispensable contribution for the future research about these phases. The size and morphology of gallium ferrite NPs were studied by transmission electron microscopy (TEM) and the organic matter on the surface of the NPs was quantified by thermogravimetric analysis. In addition, a rigorous magnetic study of the samples was performed by means of a superconducting quantum interference device (SQUID) magnetometer and Electron Magnetic Resonance (EMR). Finally, the potential application of the samples as MRI contrast agents has been explored by means of relaxivity measurements.

## 2. Experimental

### 2.1. Materials

Gallium(III) (99.99%) and iron(III) (99.99%) acetylacetonates, oleic acid (90%), oleylamine (70%), 1,2-hexadecanediol (90%) and poly(maleic anhydride-*alt*-1-octadecene) (PMAO) ( $M_w = 30\,000\text{--}50\,000$  Da) were purchased from Sigma Aldrich. Ethanol was obtained from Panreac S.A. and phosphate-buffered saline (PBS) from Gibco. The solvents toluene and dibenzyl ether (DBE) (98%) were purchased from Sigma-Aldrich and used as received without purification.

### 2.2. Synthesis of gallium-doped $\text{Fe}_3\text{O}_4$

$\text{Fe}_{3-x}\text{Ga}_x\text{O}_4$  ferrites with different amounts of gallium were synthesized by mixing stoichiometric proportions of gallium (III) and iron(III) acetylacetonates (Table S1 in the ESI<sup>†</sup>). In a three-neck flask, 3 mmol of  $\text{Ga}(\text{acac})_3$  and  $\text{Fe}(\text{acac})_3$  mixture, 4 mmol of oleic acid, 4 mmol of oleylamine, 8 mmol of 1,2-hexadecanediol and 25 mL of benzyl ether were mixed and mechanically stirred under Ar flow. The first 30 min of the reaction was maintained without heating in order to evacuate all the oxygen and water molecules present in the reaction bottle. Then, the mixture was heated to 200 °C at 4 °C  $\text{min}^{-1}$  and maintained at that temperature for 30 min (the nucleation phase). Thereafter, the temperature was raised to 300 °C, at 2.2 °C  $\text{min}^{-1}$  and maintained at reflux for 90 min (the growth phase), and the colour of the reaction mixture changed from a reddish brown to black due to the reduction process. Finally, the solution was cooled to R.T. and the nanoparticles were precipitated using ethanol and separated from the supernatant with a permanent Nd magnet. The nanoparticles were twice dispersed in toluene and precipitated in ethanol and finally resuspended in toluene. Hydrophobic dispersions of oleic acid coated  $\text{Fe}_{3-x}\text{Ga}_x\text{O}_4$  nanoparticles, with nominal compositions of  $x = 0.14, 0.3, 0.45, 0.57, 1.05$  and 1.35, were obtained and

stored in the fridge. The  $\text{GaFe}_2\text{O}_4$  phase to be used as the standard was synthesized by the sol-gel method from  $\text{Ga}_2\text{O}_3$  and  $\text{Fe}(\text{NO}_3)_3$  dissolved in  $\text{HNO}_3$  solution after adding citric acid and ethylene glycol.

### 2.3. PMAO polymer coatings for nanoparticles

The hydrophobic samples  $\text{Fe}_{3-x}\text{Ga}_x\text{O}_4$  were transferred to water by functionalization with poly(maleic anhydride-*alt*-1-octadecene) (PMAO) polymer modifying the protocol of Parak *et al.*<sup>31</sup> Thus, 2.5 mg of each sample was redispersed in 40 mL of chloroform with corresponding amounts of PMAO (100 monomers per  $\text{nm}^2$  of nanoparticles, Table S1†) and evaporated at 40 °C. Then, the hydrolysis of the anhydrous groups was carried out with a solution of standard buffer solution (SBS, pH = 9.5) at 40 °C for 1 h. Then the samples were centrifuged for 5 min at 6000 rpm and dispersed in water.

### 2.4. Physical, structural, and magnetic characterization

X-Ray Diffraction (XRD) patterns of the as-synthesized dried samples were obtained with a PANalytical X'Pert PRO diffractometer with a copper anode (operated at 40 kV and 40 mA), diffracted beam monochromator and PIXcel detector. Scans were collected in the 10–90°  $2\theta$  range, with a step size of 0.02° and scan step speed of 1.25 s. Diffraction patterns were analysed by the Rietveld profile refinement method using the FullProf program.<sup>32</sup>

An inductively coupled plasma-mass ICP-MS (7700x, Agilent Technologies) spectrophotometer was used to measure the Fe and Ga contents of the samples. The percentage of organic matter in the NPs was determined by thermogravimetric measurements performed in a NETZSCH STA 449C thermogravimetric analyser by heating 10 mg of the sample at 10 °C  $\text{min}^{-1}$  under a dry Ar atmosphere.

Dynamic light scattering (DLS) and  $\zeta$ -potential of the NPs coated with PMAO were collected using a Zetasizer Nano-ZS (Malvern Instruments). The TEM micrographs of both as-synthesized and water-stable NPs were obtained using a JEOL JEM 2010 with an accelerating voltage of 200 kV, and a point resolution of 0.19 nm, which provides morphology images and the corresponding crystal structures by selected-area electron diffraction.

XANES (X-ray absorption near edge structure) spectra were recorded at room temperature and under atmospheric conditions at the XAFS beamline (11.1R) of the Elettra synchrotron (Trieste, Italy). The beamline provides X-ray energies in the range of 2.4–27 keV using a monochromator of a double crystal of Si(111). The Fe K-edge (7112 eV) and Ga K-edge (10377 eV) absorption spectra were collected in transmission mode using ionization chambers as the detectors. Under these conditions, the edge position can be determined with an accuracy of 0.2 eV. The energy edge for each sample was calibrated by recording simultaneously the XANES spectrum of an Fe or Ga foil placed after the sample. Samples were prepared by mixing dried samples with polyvinylpyrrolidone (PVP) and compacted into 10 mm diameter pills. Data on  $\text{Ga}_x\text{Fe}_{3-x}\text{O}_4$  samples and on a series of Fe standards ( $\text{Fe}_3\text{O}_4$  (magnetite)

and  $\text{Fe}_2\text{GaO}_4$  (Ga-ferrite)) and Ga oxides ( $\beta\text{-Ga}_2\text{O}_3$ ) were collected. Spectra were measured up to  $k = 14 \text{ \AA}^{-1}$  at the Fe K-edge and up to  $k = 12 \text{ \AA}^{-1}$  at the Ga K-edge with a high signal-to-noise ratio. Two spectra were acquired and averaged for each sample to improve the signal-to-noise ratio. Spectra were analysed using the Athena software from the Iffefit package.<sup>33</sup>

Quasi-static magnetization measurements as a function of magnetic field,  $M(H)$ , and temperature,  $M(T)$ , were carried out using a SQUID magnetometer (MPMS3, Quantum Design). These measurements were performed by drying colloids of NPs ( $\sim 0.1 \text{ mg mL}^{-1}$ ) on semipermeable filter paper. The saturation magnetization,  $M_s$ , at RT and 5 K was obtained from the dried as-synthesized samples (powder) and normalized per unit mass of inorganic matter by subtracting the weight percentage of organic matter determined by thermogravimetry.

The cytotoxicity assay was performed on the human colorectal cancer cell line HCT116 (ATCC), which was cultured in Dulbecco's Modified Eagle's Medium (DMEM) (Gibco) and supplemented with 10% FBS and antibiotics at 37 °C and under 5%  $\text{CO}_2$  atmosphere. Cells were seeded in 96-well plates at a density of 1000 cells per well and allowed to attach to the plate before the addition of nanoparticles. After attachment, 0.1  $\mu\text{g}$  ( $C_1 = 0.1 \text{ ng}_{\text{NP}}$  per cell) and 1  $\mu\text{g}$  ( $C_2 = 1 \text{ ng}_{\text{NP}}$  per cell) of NPs per well [UdMO1] were added. Proliferation was measured at days 0, 1, 2, 3 and 4. For crystal violet staining, cells were fixed in 4% paraformaldehyde and stained with 0.1% crystal violet. After staining, cells were washed and 10% acetic acid was added. Absorbance was measured at 590 nm.

Magnetic relaxivity measurements were performed using a Bruker Minispec MQ60 instrument (Bruker Biospin GmbH, Ettlingen, Germany) at 37 °C. All experiments were performed using a volume of 300  $\mu\text{L}$  of a dispersion of the ferrites in water. The longitudinal relaxation times ( $T_1$ ) and the transversal relaxation times ( $T_2$ ) were determined using an inversion-recovery (IR) and the Carr-Purcell-Meiboom-Gill (CPMG) methods, respectively. The measurements were performed at five different gallium concentrations (0.05, 0.1, 0.20, 0.25 and 0.35 mM Ga) in aqueous solution and three different times for statistical correction. The final relaxivities ( $r_1$  and  $r_2$ ) were calculated from the slope of the linear fit of the inverse of the relaxation times against the millimolar concentration of Ga.

## 3. Results and discussion

### 3.1. Structural and morphological characterization of the samples

Gallium-doped ferrite nanoparticles were synthesized by the thermal decomposition method by adjusting the amount of gallium and iron precursors desired in each synthesis [Table S1†]. Following this method, dispersions of  $\text{Fe}_{3-x}\text{Ga}_x\text{O}_4$  ( $0.14 \leq x \leq 1.35$ ) nanoparticles surrounded by oleic acid and oleylamine were obtained. Some of the samples ( $\text{Fe}_{3-x}\text{Ga}_x\text{O}_4$ ,  $x = 0.14, 0.26$  and  $0.57$ ) were water-transferred by functionalization with the amphiphilic polymer PMAO in order to study the biological viability and the possibility to be used as con-

trast agents in MRI. The real contents of gallium and iron were calculated by ICP-AES, showing gallium percentages between 4.9 and 45% ( $0.14 \leq x \leq 1.35$ ), quite near to the theoretical values employed in the synthesis. In Table 1, the calculated formula from the chemical analysis has been included. As mentioned previously, the nanoparticles were prepared in the presence of organic ligands, so the amounts of the surrounding oleic acid and oleylamine for the nanoparticles employed in this study have been deduced from the thermogravimetric curves performed in an Ar atmosphere (Fig. S1†). Although decompositions performed in an air atmosphere would yield a complete and cleaner decomposition of the organic groups, oxidation processes of the inorganic core would also occur. Thermogravimetric curves show two abrupt weight losses corresponding to the coating ligands, and a slight decomposition up to 200 °C of the residual solvents can be observed. The significant loss at  $\approx 350$  °C is related to decomposition of the weakly attached surface functional coating or capping molecules (oleic acid molecules and oleylamine) as the boiling temperatures of oleic acid (OA) and oleylamine (OLA) are 360 °C and 364 °C, respectively. The mass loss above 600 °C can be attributed to the decomposition of tightly linked molecules or intermediate iron carbonates, together with a process of evolution of the ferrite inorganic core.<sup>34,35</sup> Weight losses corresponding to the organic matter vary from one sample to another in the range 15–42% (Table 1) with these differences being related not only to NP size but also to the particle washing process or to the relationship with the metal precursors. First of all, the amounts of the gallium precursor used in the syntheses vary due to the different thermal decomposition window for each precursor and the nucleation and growth kinetics change from one sample to another which, in turn, would affect the tendency of the surfactant to be bound to the nanoparticle surface.<sup>36</sup> Secondly, as the gallium precursor amounts vary, so does the crystallite size calculated by X-ray diffraction (5–9 nm). Smaller nanoparticles with larger surface areas provide more surface binding sites than larger NPs, so higher amounts of ligands should be attached to particles with smaller sizes.<sup>37</sup> Finally, the precipitation and washing processes performed lead to different amounts of ligands surrounding the inorganic nuclei. All these processes determine

the organic loading observed, thus making it impossible to attribute only to particle size effects.

The structural characteristics of the samples have been analysed by X-ray diffraction (XRD). The patterns of the samples consist of broad and not very well-resolved peaks because of the small size of the crystallite domain and the amount of organic matter covering the nanoparticles (Fig. 1). The peaks and intensities match well for the inverse spinel structure of magnetite ( $Fd\bar{3}m$ , JPCDS no. 89-0691) with no trace of secondary phases as was deduced after the Rietveld refinements. The crystallite size was calculated using Scherrer's formula from the (3 1 1) and (4 0 0) reflections as the broadness of the (3 1 1) diffraction peak could include a part of the intensity of (2 2 2) leading to inaccurate results (Fig. 1b) (Table S2 in the ESI†).<sup>38</sup> The refined structural data from the Rietveld calculation are shown in the ESI† (Fig. S2 and Table S3 in the ESI†) and included in Table 1 as the calculated lattice parameter. These parameters vary from 8.376(3) Å for the samples with lower Ga contents to 8.360(3) Å for samples with the highest percentage of Ga. Although a linear variation of the cell parameter with the increasing content of gallium is not accurately observed probably due to the low quality of the diffraction patterns, a continuous decrease in the parameter can be gathered (Fig. 1c). These decreasing values are in good accord with the lattice parameter observed for other Ga-doped ferrites in the literature.<sup>39</sup> Furthermore, considering the size and charge of gallium cations ( $d^{10}$ ), it should be expected to occupy the positions of  $Fe^{3+}$  ions with no special preference for tetrahedral or octahedral positions. According to V. L. Pool *et al.*, in concentrations less than 20%,  $Ga^{3+}$  ions tend to occupy tetrahedral positions of the spinel structure.<sup>28</sup> However, other studies demonstrate the random distribution of  $Ga^{3+}$  between the tetrahedral and octahedral positions, which would also result in a nonlinear evolution of the cell parameters with gallium content.<sup>40,41</sup>

Regarding the morphological analysis of the samples, transmission electron microscopy (TEM) showed similar morphologies (cuboctahedrons) and sizes in the 6–12 nm range, as can be seen in Fig. 2. The measured sizes are rather compatible with those previously calculated from XRD data by the Scherrer equation, meaning that the NPs are mainly composed of single crystals. Similar characteristics in all the nanoparticles are expected as the same reaction conditions have been employed in all the syntheses, mainly the same amount of oleic acid.<sup>42</sup> Nevertheless, a more detailed observation of the micrographs shows that for lower gallium contents, nanoparticles are less faceted and as the content of  $Ga^{3+}$  increases, bigger sizes and more prismatic (cuboctahedrons and truncated octahedrons) particles are observed. Probably, the presence of a higher concentration of the  $Ga(acac)_3$  precursor in the synthesis that decomposes at 198 °C, which is 18 °C higher than the decomposition temperature for  $Fe(acac)_3$ , could delay the nucleation process, thus shaping the growth of the particles.

### 3.2. X-Ray absorption near edge structure (XANES)

Although there is evidence of the evolution of crystallographic parameters with Ga content, characterization of the nanoparticles by means of XANES could provide complementary

**Table 1** Summary of the chemical and structural data in  $Fe_{3-x}Ga_xO_4$  ( $0.14 \leq x \leq 1.35$ ) samples: formula calculated from ICP analysis, percentage of organic matter (O.M.), size of the crystalline domain ( $D_{DRX}$ ) by the Scherrer calculation from (3 1 1) and (4 0 0) reflections and particle mean diameter obtained by TEM ( $D_{TEM}$ ) and 'a' structural parameter from the Rietveld refinement

Sample	O.M. (%)	$D_{DRX}$ (nm) mean size 311–400	$D_{TEM}$ (nm)	$a$ (Å)
$Fe_{2.86}Ga_{0.14}O_4$	42	5(1)	$6.8 \pm 1.0$	8.376(4)
$Fe_{2.73}Ga_{0.27}O_4$	32	6(1)	$9.1 \pm 1.7$	8.380(3)
$Fe_{2.55}Ga_{0.45}O_4$	33	6(1)	$8.9 \pm 5.0$	8.374(4)
$Fe_{2.42}Ga_{0.57}O_4$	15	7(1)	$9.8 \pm 2.3$	8.378(2)
$Fe_{1.95}Ga_{1.05}O_4$	16	9(1)	$7.8 \pm 1.2$	8.359(2)
$Fe_{1.65}Ga_{1.35}O_4$	28	7(1)	$8.7 \pm 1.1$	8.360(3)

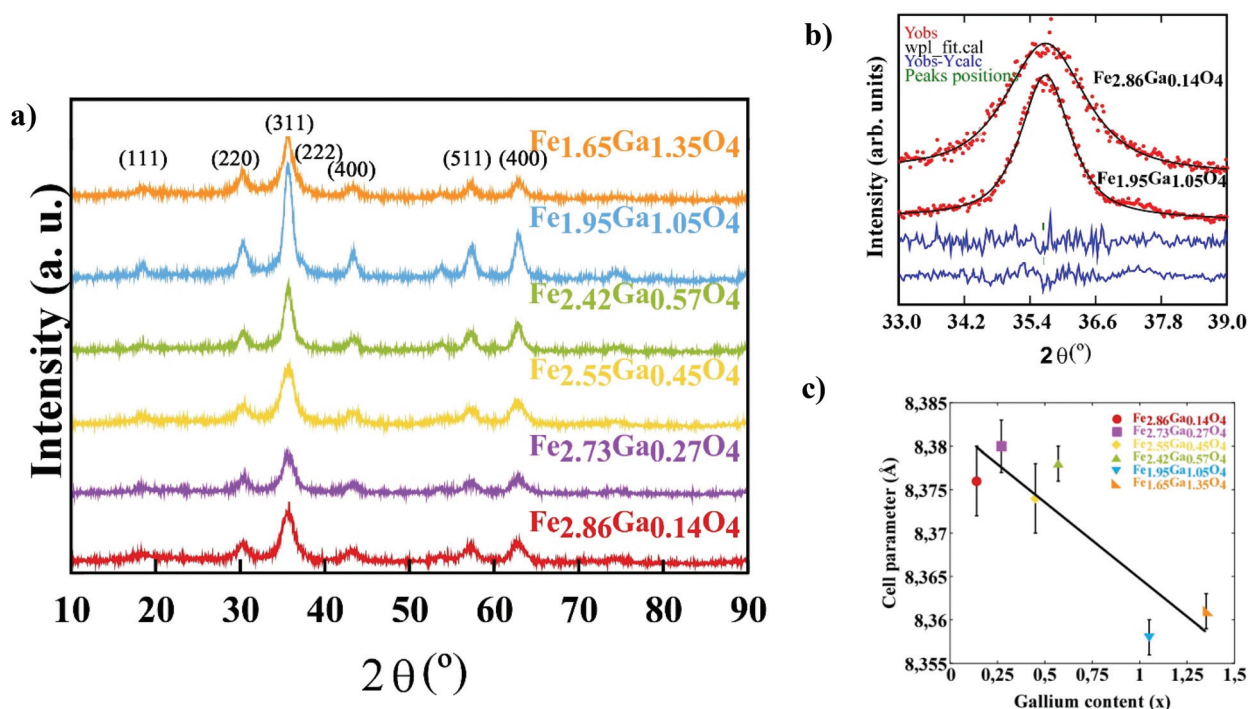


Fig. 1 (a) X-ray powder diffraction patterns of the  $\text{Fe}_{3-x}\text{Ga}_x\text{O}_4$  ( $0.14 \leq x \leq 1.35$ ) samples. (b) Zoom of the (311) diffraction peak and (c) lattice parameter 'a' obtained by Rietveld refinement versus Ga-content (x) estimated by ICP-MS.

information about metal oxidation states and site symmetry of the cations.<sup>43</sup> For this purpose, XANES spectra at the Fe and Ga K-edges on  $\text{Fe}_{3-x}\text{Ga}_x\text{O}_4$  and different standards have been recorded using an Elettra synchrotron. Fig. 3 shows the XANES spectra after background subtraction and data normalization.<sup>44</sup> As has been previously mentioned, magnetite is an inverse spinel where the Fe ions occupy three different sites: 8  $\text{Fe}^{2+}$  in octahedral sites, 8  $\text{Fe}^{3+}$  in tetrahedral sites, and 8  $\text{Fe}^{3+}$  in octahedral ones. In contrast, Ga-ferrite ( $\text{Fe}_2\text{GaO}_4$ ) is mostly normal spinel in which the  $\text{Ga}^{3+}$  cations mainly occupy the tetrahedral sites and partially the octahedral ones while the  $\text{Fe}^{2+}$  and  $\text{Fe}^{3+}$  cations are located in the octahedral sites in coexistence with some  $\text{Fe}^{3+}$  in tetrahedral coordination.<sup>30</sup>

Different features should be analysed in the XANES spectra to obtain information on the oxidation state and symmetry of the absorber: the edge position (defined as the energy at which the value of the normalized absorption coefficient is 0.5), the pre-edge and the post-edge regions.

According to the Fe K-edge position, slight displacements are noted between both samples. While the edge position of magnetite appears at 7124.3 eV, it is shifted 1.1 eV to lower energies for the prepared  $\text{Fe}_2\text{GaO}_4$  sample (7123.2 eV) (Fig. 3a). The edge position is a clear-cut indicator of the oxidation state, thus, the edge position displaces 7 eV to lower energies when the oxidation state decreases from  $\text{Fe}^3$  to  $\text{Fe}^{2+}$ .<sup>45,46</sup> Both magnetite and  $\text{Fe}_2\text{GaO}_4$  present a mixed valence state where the  $\text{Fe}^{2+}:\text{Fe}^{3+}$  ratio varies from 1:2 (magnetite) to 1:1 ( $\text{Fe}_2\text{GaO}_4$ ) and so, the observed 1.1 eV energy shift agrees with the relative decrease of  $\text{Fe}^{3+}$  in the Ga-ferrite.

Secondly, notable changes are observed in the shoulder presented  $\sim 10$  eV below the edge position. This pre-edge peak is attributed to the electronic transitions from the 1s core state to the 3d, forbidden by the dipole selection rules and the intensity and position provides information about the symmetry of the absorbing atom.<sup>45,47</sup> The  $\text{Fe}_2\text{GaO}_4$  Fe K-edge XANES spectrum presents a broad and less intense pre-edge peak, characteristic of a centrosymmetric environment of the Fe absorbing atoms which are mostly located in octahedral coordination. In contrast, magnetite presents a narrower and more intense peak, confirming the presence of non-centrosymmetric sites characteristic of tetrahedral coordination. Finally, the post-edge region manifests the differences in the medium-range order of the absorber atoms in magnetite and  $\text{Fe}_2\text{GaO}_4$ .<sup>43,48,49</sup>

The  $\text{Fe}_{3-x}\text{Ga}_x\text{O}_4$  samples ( $x = 0.14, 0.27, 0.54$  and  $0.57$ ) display very similar spectra to the one of magnetite. Regarding the edge position, a slight displacement of 0.3 eV towards lower energies is observed for samples  $\text{Fe}_{2.86}\text{Ga}_{0.14}\text{O}_4$  and  $\text{Fe}_{2.73}\text{Ga}_{0.27}\text{O}_4$ , corresponding with the expected Ga concentration  $x \approx 0.2-0.3$ . In contrast, for  $\text{Fe}_{2.46}\text{Ga}_{0.54}\text{O}_4$  and  $\text{Fe}_{2.42}\text{Ga}_{0.57}\text{O}_4$  the edge positions just shifted 0.2 eV (within the error) when higher displacements should be expected according with the Ga concentrations obtained by ICP. The non-linearity of the edge position with the increasing Ga content could suggest the existence of some  $\text{Fe}^{2+}$  vacancies which would modify the  $\text{Fe}^{2+}:\text{Fe}^{3+}$  ratio, as has been previously observed,<sup>50</sup> considering that no secondary phases are detected in X-ray diffraction (Fig. 1). The pre-edge region reproduces the energy shift-tendency observed in the edge position as the presence of

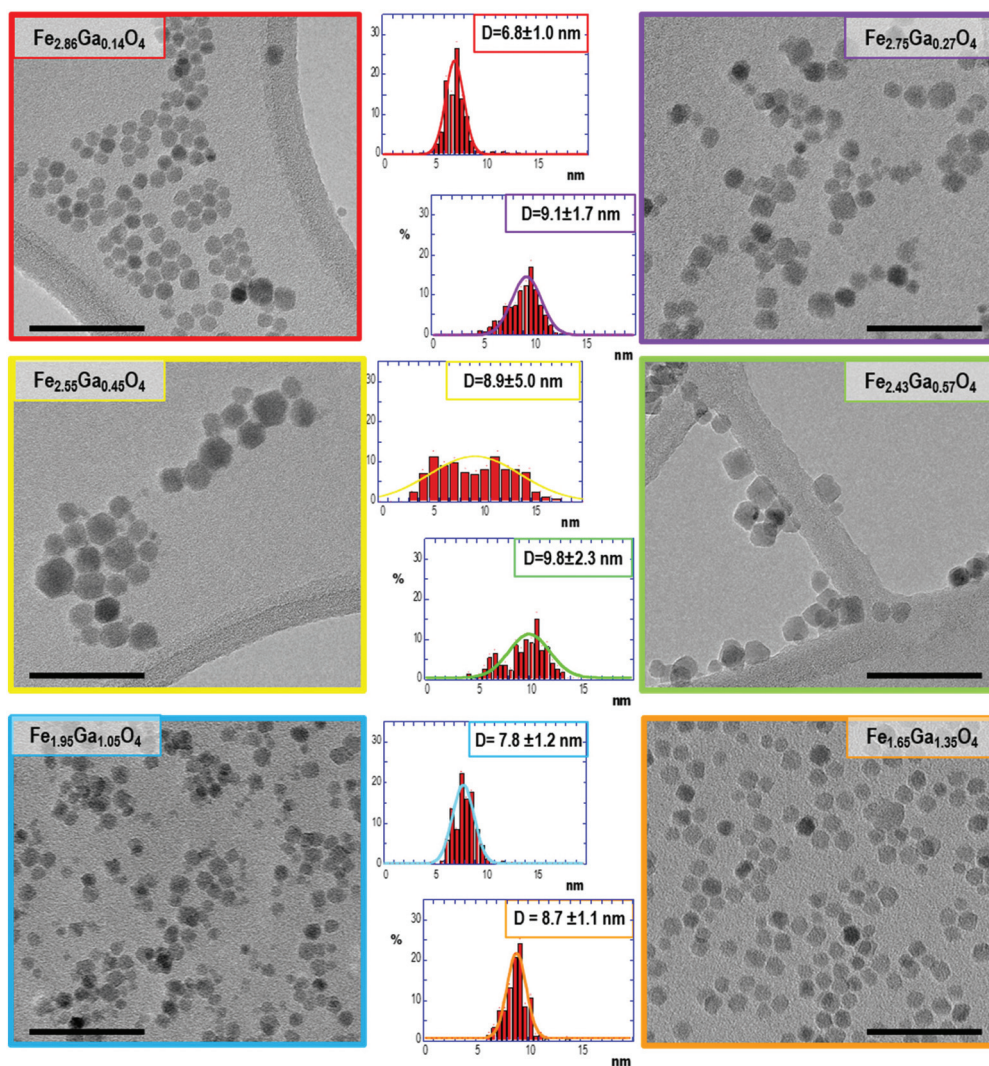


Fig. 2 TEM images of samples and their log norm size distribution for  $\text{Fe}_{3-x}\text{Ga}_x\text{O}_4$  ( $0.14 \leq x \leq 1.35$ ) samples. Scale bar = 50 nm.

Ga in the  $\text{Fe}_{3-x}\text{Ga}_x\text{O}_4$  samples barely alters the shape and intensity of the pre-peak compared to magnetite.

Ga K-edge XANES spectra of the  $\text{Fe}_{3-x}\text{Ga}_x\text{O}_4$  samples are observed in Fig. 3c, together with the one of  $\beta\text{-Ga}_2\text{O}_3$  and  $\text{Fe}_2\text{GaO}_4$ . These spectra, which exhibit a good signal-to-noise ratio, confirm the presence of Ga in the samples. The edge position of the synthesized nanoparticles is coincident with the one observed in both  $\beta\text{-Ga}_2\text{O}_3$  and  $\text{Fe}_2\text{GaO}_4$  XANES spectra, revealing that the oxidation state of the Ga atoms is  $\text{Ga}^{3+}$ . The main differences between the samples, and with respect to the Ga reference oxides, appear in the white line region. Above the edge position, all spectra show a wide white line with a double shoulder feature, wherein the relative intensity between those shoulders varies progressively between samples. According with the literature, this double shoulder feature, observed in  $\beta\text{-Ga}_2\text{O}_3$ , is attributed to a mixed  $\text{Ga}^{3+}$  environment.<sup>51,52</sup> On the one hand, the existence of tetrahedrally coordinated  $\text{Ga}^{3+}$  gives rise to the low energy peak centered around 10 379 eV, while the high energy peak, at  $\sim 10 382$  eV, is attributed to the

$\text{Ga}^{3+}$  ions occupying octahedral sites. In this way, it can be deduced that despite a mixed environment of  $\text{Ga}^{3+}$  ions in the  $\text{Fe}_{3-x}\text{Ga}_x\text{O}_4$  samples, for low gallium concentrations (as  $x = 0.14$ ),  $\text{Ga}^{3+}$  preferentially occupies tetrahedral positions and the first shoulder is the most intense. As  $\text{Ga}^{3+}$  content increases, the tetrahedral/octahedral ratio progressively decreases until reaching the situation of the  $\text{Fe}_2\text{GaO}_4$  ferrite, with an already significant tetrahedral occupation of gallium, as previously extracted from the pre-peak information on the Fe K-edge.

The evolution of the XANES spectra suggests that Ga and Fe ions occupy both tetrahedral and octahedral sites, but with a variable relation  $\text{Ga}^{\text{Td}}/\text{Ga}^{\text{Oh}}$  depending on the increasing amounts of gallium in the samples.

### 3.3. Magnetic characterization

The influence of the Ga content on the magnetic behavior of the nanoparticles has been analyzed by performing magnetization measurements with the magnetic field,  $M(H)$ , and the

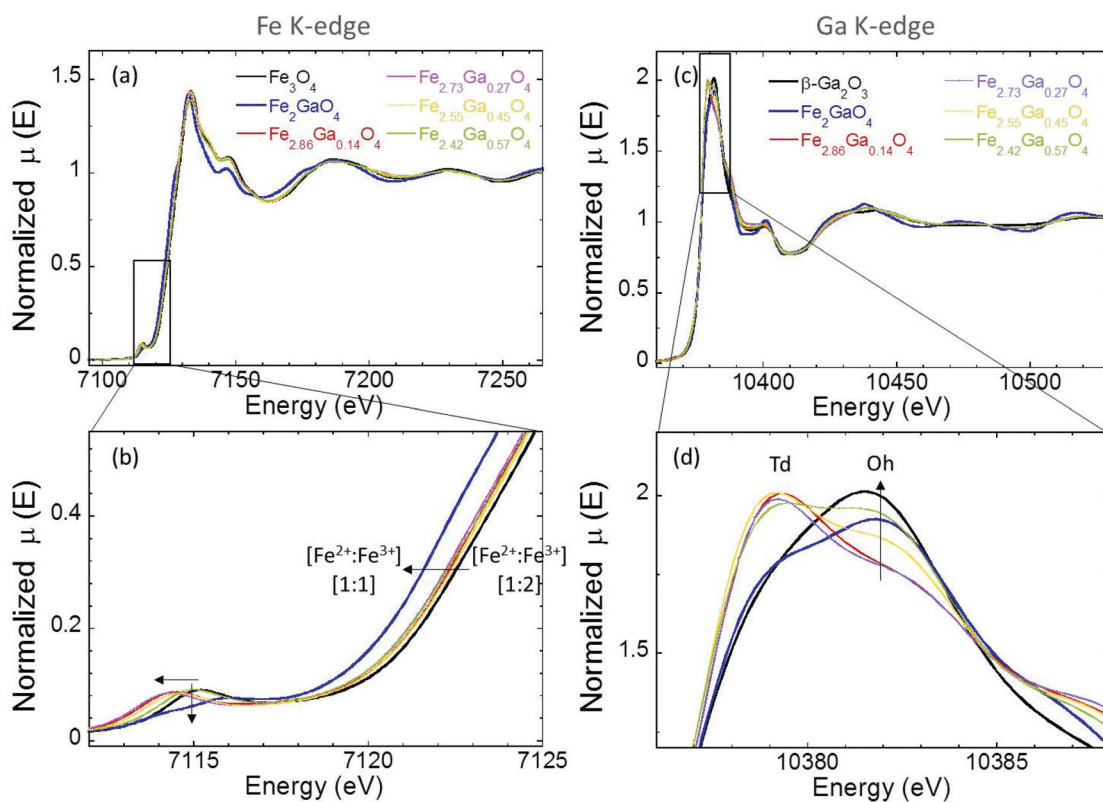


Fig. 3 (a) Normalized XANES spectra of the  $\text{Fe}_{3-x}\text{Ga}_x\text{O}_4$  sample ( $x = 0.14, 0.27, 0.45$  and  $0.57$ ) nanoparticles compared to reference compounds: magnetite ( $\text{Fe}_3\text{O}_4$ ) and Ga-ferrite ( $\text{Fe}_2\text{GaO}_4$ ). (b) Inset of the pre-edge region compared in (a). (c) Ga K-edge XANES spectra of  $\text{Fe}_{3-x}\text{Ga}_x\text{O}_4$  samples compared to  $\text{Fe}_2\text{GaO}_4$  and  $\text{Ga}_2\text{O}_3$ . (d) Zoom-in of the with-line region compared in (c).

temperature,  $M(T)$ . The  $M(H)$  curves at 300 K and 5 K are shown in Fig. 4. At room temperature, superparamagnetic behavior (SPM) can be confirmed by the absence of coercivity ( $H_c$ ) and remanence ( $M_r$ ) in agreement with the small sizes of the nanoparticles. Otherwise, at 5 K nanoparticles show hysteresis with full magnetization at fields  $\approx 0.5$  mT. The saturation magnetization ( $M_s$ ) of the NPs corresponds to the magnetic core since the mass has been corrected subtracting the amount of organic matter in the samples (see Fig. S1†). It is

worth mentioning that the increase of  $M_s$  values with decreasing Ga content in the samples, reaching a maximum value of  $110(1) \text{ Am}^2 \text{ kg}^{-1}$  at 5 K for a doping of  $x = 0.14$ , is significantly higher to that of pure bulk magnetite ( $98 \text{ Am}^2 \text{ kg}^{-1}$  at 5 K). This variation in magnetization could also be related to nanoparticle size. The slightly lower bonding energy of  $\text{Ga}^{3+}\text{-O}$  ( $374 \text{ kJ mol}^{-1}$ ) compared to  $\text{Fe}^{3+}\text{-O}$  ( $407 \text{ kJ mol}^{-1}$ ) should be considered for the increase in size of the  $\text{Ga}_x\text{Fe}_{3-x}\text{O}_4$  nanoparticles as less energy should be necessary to form  $\text{Ga}^{3+}\text{-O}^{2-}$

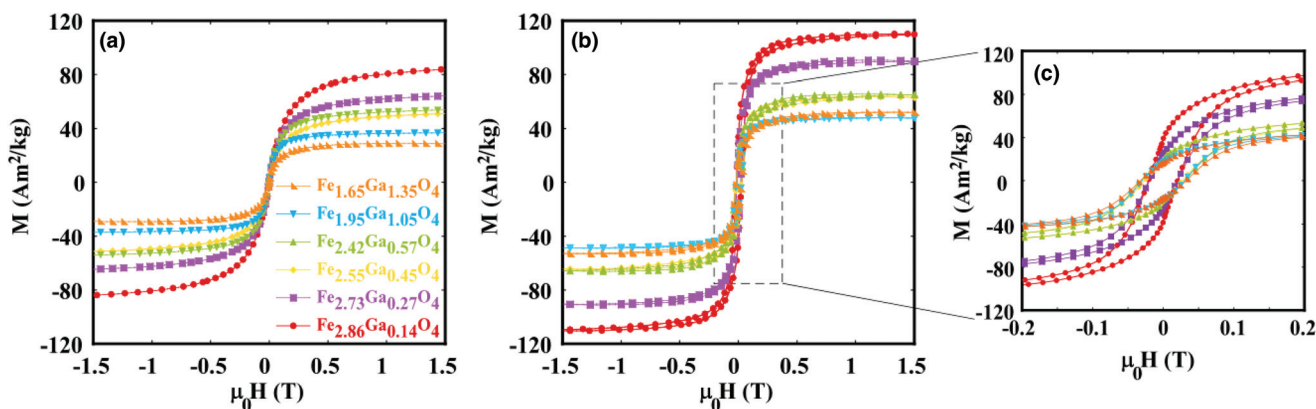


Fig. 4  $M(H)$  curves of the samples at (a) 300 K (b) 5 K and (c) inset of the low field region at 5 K.

bonds, thus accelerating the growth of nanoparticles.<sup>53,54</sup> The saturation magnetization gradually decreases with an increase in the amount of dopant, and so, with increasing particle size. Magnetic and structural studies performed on Ga ferrites have shown that both  $\text{Fe}^{3+}$  and  $\text{Ga}^{3+}$  ions can be present in both A or B positions,<sup>28,29,30</sup> a fact that has been confirmed by XANES spectroscopy earlier in the study. The distribution of gallium in the nanoparticles with the lowest doping ( $x = 0.14$ ) seems to be favoured in the tetrahedral holes, thus increasing their magnetic saturation value at low temperatures. However, as the nanoparticle size and doping increase, as shown in Fig. 3d, the distribution of gallium varies, being able to be placed indistinctly between the tetrahedral and octahedral gaps. Decompensation of the moments in the ferrimagnetic network occurs, which induces the progressive reduction of the magnetic saturation. In addition, the incorporation of doping into the magnetite phase can bring about a lack of balance of the interactions exchanged by the magnetic ions on the surface of the particles, which would also affect their magnetic properties.<sup>55</sup> For this reason, it is believed that the larger the nanoparticle size, the more noticeable the surface disorder and the greater the alteration in the magnetic properties, with all these facts being consequently related to the gallium amount. Specifically, the saturation magnetization at RT drops from  $85 \text{ Am}^2 \text{ kg}^{-1}$  in sample  $\text{Fe}_{2.86}\text{Ga}_{0.14}\text{O}_4$  to  $29 \text{ Am}^2 \text{ kg}^{-1}$  for  $\text{Fe}_{1.65}\text{Ga}_{1.35}\text{O}_4$ . Thus, it can be concluded that moderate Ga contents ( $x \approx 0.14$ ) are more suitable to maximize the saturation magnetization in this kind of  $\text{Fe}_{3-x}\text{Ga}_x\text{O}_4$  NP.

Regarding the coercivity of the samples at 5 K, the values vary between 20 and 32 mT, which are in the range of soft ferrite nanoparticles of similar sizes.<sup>56</sup> The lower  $H_c$  value (20 mT) in the  $\text{Fe}_{2.86}\text{Ga}_{0.14}\text{O}_4$  sample is likely related to its smaller average dimension ( $\approx 6 \text{ nm}$ ) and, thus, to the more sig-

nificant thermal effects. The reduced remanence ( $M_r/M_s$ ) values at 5 K in all the samples are around 0.3, which significantly deviates from the 0.5 value that the Stoner–Wohlfarth model predicts for uniaxial single domains. This is also an effect of the thermal fluctuations of the magnetic moments, which are not negligible (even at low T) for NPs smaller than 10 nm.

The size of the magnetic core in the different  $\text{Fe}_{3-x}\text{Ga}_x\text{O}_4$  samples can be also estimated using the non-interacting SPM model on the  $M(H)$  curves at RT. The magnetization of the sample can be expressed by eqn (1) where we have considered a diameter ( $D$ ) Gaussian distribution function ( $f(D)$ ).

$$M(H) = M_s(\text{emu g}^{-1}) \times \int_0^{\text{max}} L\left(\frac{M(\text{emu cm}^{-3})V(\text{cm}^3)H(\text{Oe})}{k_B T(\text{erg})}\right) f(D) dD \quad (1)$$

where  $M_s$  is the saturation magnetization and  $L(x)$  is the Langevin function. In this way, this quantitative approach provides the mean size and dispersity of the inorganic core. Fig. 5 displays the experimental  $M(H)$  curves of the samples  $\text{Fe}_{2.86}\text{Ga}_{0.14}\text{O}_4$  and  $\text{Fe}_{1.95}\text{Ga}_{1.05}\text{O}_4$  together with their corresponding fits (straight lines), performed by fixing the  $M_s$  parameter to the experimental value of each sample.  $M(H)$  fittings for the other samples are provided in Fig. S3 in the ESI.† The obtained sizes and deviations have been summarized in Table 2, which are pretty compatible with the average dimensions obtained by TEM and DRX.

The magnetization measurements *versus* temperature after zero field cooling (ZFC) and field cooling (FC) were performed under a constant magnetic field of 10 Oe (Fig. 6). All the samples present the typical profile of superparamagnetic NPs where the ZFC branch presents a maximum associated with

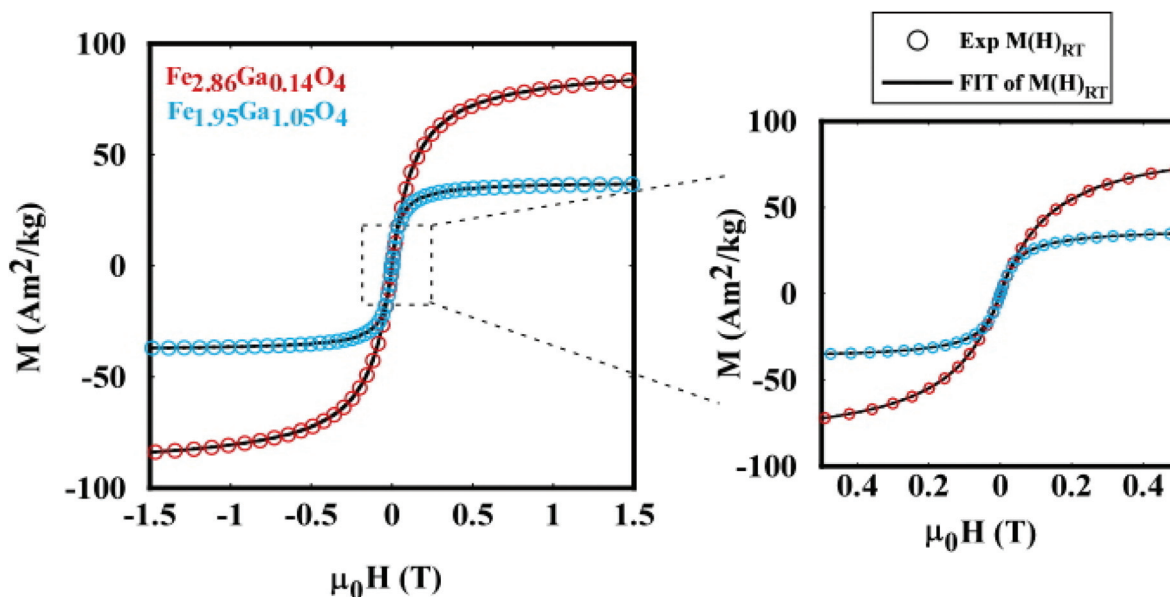
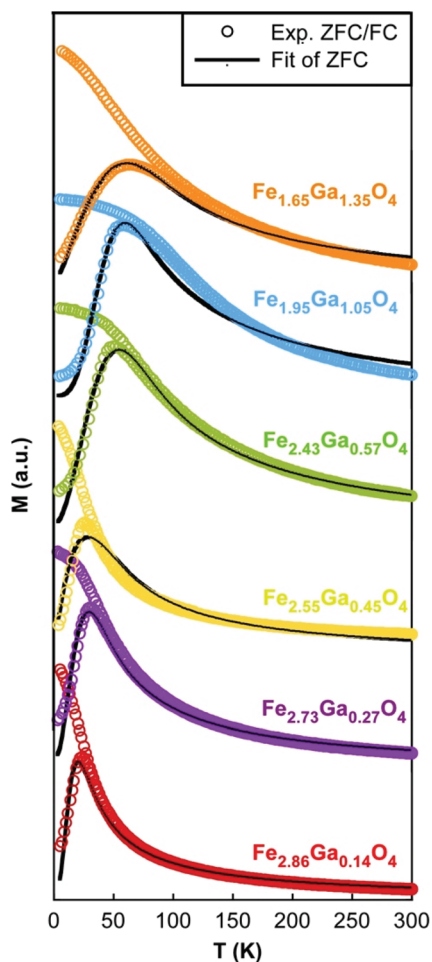


Fig. 5 Fit of  $M(H)$  curves at R.T. for  $\text{Fe}_{2.86}\text{Ga}_{0.14}\text{O}_4$  and  $\text{Fe}_{1.95}\text{Ga}_{1.05}\text{O}_4$  samples by the SPM model. The fits of the rest of the samples are displayed in the ESI (Fig. S3†).

**Table 2** Summary of saturation magnetization ( $M_s$ ), coercivity ( $H_c$ ) and reduced remanence ( $M_r/M_s$ ) of the nanoparticles obtained from the hysteresis loops at 300 K and 5 K, average magnetic diameters ( $D$ ) and dispersity ( $\sigma$ ) obtained by the fit of  $M(H)$  curves at RT and by the fit of the ZFC branch. The average blocking temperature ( $\langle T_B \rangle$ ) and the effective magnetic anisotropy constant ( $K_{\text{eff}}$ ) obtained from  $\langle T_B \rangle$

Sample	$D_{\text{DRX}}$ (nm)	$D_{\text{TEM}}$ (nm)	$M_s$ RT ( $\text{Am}^2 \text{kg}^{-1}$ )	$M_s$ 5 K ( $\text{Am}^2 \text{kg}^{-1}$ )	$M_r/M_s$ 5 K	$H_c$ 5 K (mT)	$D_{M(H)RT \pm \sigma}$ (nm)	$D_{\text{ZFC} \pm \sigma}$ (nm)	$K_{\text{effZFC}, T=0}$ ( $\text{kJ m}^{-3}$ )	$K_{\text{eff}} \langle T_B \rangle$ ( $\text{kJ m}^{-3}$ )	$\langle T_B \rangle$ (K)
$\text{Fe}_{2.86}\text{Ga}_{0.14}\text{O}_4$	5(1)	$6.8 \pm 1.0$	85(1)	110(1)	0.35(2)	20.7(1)	$5.9 \pm 1.1$	$7.2 \pm 1.1$	22.0	25.1	16.3
$\text{Fe}_{2.73}\text{Ga}_{0.27}\text{O}_4$	6(1)	$9.1 \pm 1.0$	65(1)	90(1)	0.27(2)	19.9(1)	$6.9 \pm 2.3$	$7.5 \pm 1.3$	28.9	25.4	23.4
$\text{Fe}_{2.55}\text{Ga}_{0.45}\text{O}_4$	6(1)	$8.9 \pm 5.0$	52(1)	64(1)	0.30(2)	26.6(1)	$7.3 \pm 2.8$	$7.5 \pm 2.1$	20.1	19.8	18.6
$\text{Fe}_{2.42}\text{Ga}_{0.57}\text{O}_4$	8(1)	$9.8 \pm 2.3$	54(1)	65(1)	0.28(2)	31.0(1)	$8.3 \pm 2.9$	$9.7 \pm 2.0$	22.6	20.2	34.4
$\text{Fe}_{1.95}\text{Ga}_{1.05}\text{O}_4$	9(1)	$7.8 \pm 1.6$	37(1)	48(1)	0.37(2)	30.0(1)	$11.0 \pm 2.9$	$12.3 \pm 1.8$	14.1	12.7	40.5
$\text{Fe}_{1.65}\text{Ga}_{1.35}\text{O}_4$	7(1)	$7.4 \pm 1.0$	29(1)	52(1)	0.31(2)	32.3(1)	$10.8 \pm 2.8$	$11.3 \pm 3$	13.1	12.6	41.4



**Fig. 6** Experimental ZFC/FC measurements at 10 Oe (circular markers) with the fit of the ZFC branch (solid line) for the  $\text{Fe}_{3-x}\text{Ga}_x\text{O}_4$  set of samples.

the blocking temperature ( $T_B$ ) of the system while the FC branch shows a continuous increase in magnetization from R. T. to low temperatures.<sup>57</sup>

Although the maximum of the ZFC curve is usually assumed to be the  $T_B$  of the system, it is more accurate to calculate the average  $T_B$ ,  $\langle T_B \rangle$ . This requires the estimation of the distribution of energy barriers  $f(T_B)$  (Fig. S4† in the ESI).<sup>58,59</sup> In this way, more reliable  $\langle T_B \rangle$  values can be obtained (see Table 2), which

also leads to a more realistic estimation of the effective anisotropy constant  $K_{\text{eff}}$  (by the widely known eqn (2)).

$$T_B = \frac{K_{\text{eff}}V}{25 k_B} \quad (2)$$

As can be observed in Table 2,  $\langle T_B \rangle$  values tend to become larger with the increasing average size of the samples, ranging from 16 to 40 K. These values are lower than those observed for magnetite NPs of similar sizes,<sup>60</sup> probably because of the softening effect of  $\text{Ga}^{3+}$  ions in the structure. This effect can also be deduced from the lower  $K_{\text{eff}}$  values obtained in samples with larger gallium amount. It should be pointed out that  $K_{\text{eff}}$  estimated from the  $\langle T_B \rangle$  values represent the anisotropy at temperatures close to the ZFC maximum, so they should be somewhat lower than the  $K_{\text{eff}}$  values at low  $T$  ( $\approx 5$  K) due to the thermal dependence of the magnetic anisotropy.  $K_{\text{eff}}$  values at 5 K can be obtained by fitting the ZFC branches within the framework of the Stoner–Wohlfarth model,<sup>61</sup> which accounts for the contribution of both the SPM NPs and the blocked NPs (see eqn (3)):

$$M_{\text{ZFC}} = \int_0^{V_c} M^{\text{SPM}} f(D) dD + \int_{V_c}^{\infty} M_{\text{ZFC}}^{\text{bl}} f(D) dD \quad (3)$$

$$M_{\text{ZFC}}^{\text{bl}} = M_s \frac{MH}{3K} \quad V_c = \frac{25 k_B T}{K}$$

The fits of ZFC branch of the whole set of  $\text{Fe}_{3-x}\text{Ga}_x\text{O}_4$  samples are presented in Fig. 6 by straight black lines. These fits not only provide a value for the anisotropy constant at low temperature but also the mean diameter and its standard deviation (summarized in Table 2). The  $K_{\text{eff}}$  at low  $T$  are in accordance with the  $K_{\text{eff}}$  values estimated from the  $\langle T_B \rangle$ , further supporting that the NPs become magnetically softer with increasing Ga contents. Moreover, the  $D$  and  $\sigma$  estimated from the ZFC fit are rather compatible with both the data extracted from the  $M(H)$  curve fittings (Fig. 5) and the average dimensions obtained from TEM and DRX analyses (see Table 2), making these sets of outcomes fairly consistent.

Electron magnetic resonance (EMR) measurements were carried out to obtain complementary information for the magnetic behaviour. Fig. 7 shows the EMR spectra recorded for the  $\text{Fe}_{3-x}\text{Ga}_x\text{O}_4$  samples in toluene colloidal dispersions. Samples of magnetite nanoparticles, with homogeneous size, shape, and composition, are characterized by unique and well-

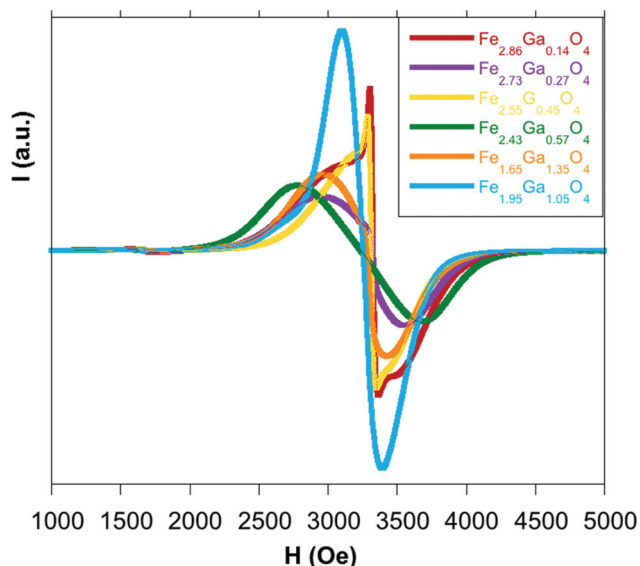


Fig. 7 Room temperature EMR spectra obtained at a frequency of 9.40 GHz for cleaned samples in toluene dispersions.

resolved lines with a  $g$  factor = 2 when nanoparticles are small. It has been previously observed that both the broadness of the line and the value of the resonant line,  $H_r$ , vary for magnetite NPs from one sample to another and that this variation is strongly correlated with the degree of alignment of the internal spin towards the applied magnetic field, that is, it depends on the nanoparticle size.<sup>60</sup>

In accordance with these approaches, the spectra of the  $\text{Fe}_{3-x}\text{Ga}_x\text{O}_4$  nanoparticles were analysed and two kinds of spectra were observed. The samples  $\text{Fe}_{3-x}\text{Ga}_x\text{O}_4$  ( $x = 0.57, 1.05, 1.35$ ) show broad and symmetric signals centered around  $g = 2.07$ . In the case of  $\text{Fe}_{1.95}\text{Ga}_{1.05}\text{O}_4$  and  $\text{Fe}_{1.65}\text{Ga}_{1.35}\text{O}_4$ , the smaller bandwidths of the spectra ( $\Delta H_{pp}$ ) are indicative of NPs of homogeneous distribution of nanoparticles with smaller sizes, in accordance with the narrow size distribution observed in the TEM histograms (Fig. 2), which is more obvious for  $\text{Fe}_{1.95}\text{Ga}_{1.05}\text{O}_4$  composition with the most symmetric and narrow signal, as can be noted in the corresponding histogram. The  $\text{Fe}_{2.42}\text{Ga}_{0.57}\text{O}_4$  sample shows resonant fields between  $H_{r\min} = 2766$  Oe and  $H_{r\max} = 3700$  Oe, which is quite a broad signal indicative of the progressive alignment of spins of nanoparticles with different sizes (Fig. 2).

For the other samples,  $\text{Fe}_{2.86}\text{Ga}_{0.14}\text{O}_4$ ,  $\text{Fe}_{2.73}\text{Ga}_{0.27}\text{O}_4$  and  $\text{Fe}_{2.55}\text{Ga}_{0.45}\text{O}_4$ , despite the spectra being centered at  $g = 2.02$  and the broadness not very noticeable, more than one component can be observed in accordance with not very homogeneous samples. The small peak appearing at  $H_r = 3300$  Oe is representative of a small population of nanoparticles with very small size ( $\approx 4$  nm), which can be observed in some of the TEM images of the samples.<sup>62</sup> The influence of the morphology and size distribution of the nanoparticles on the resonant fields of EMR signals masks the effects that could be inferred by the different gallium content in the samples.

### 3.4. Biomedical applications

After the detailed physico-chemical study of the  $\text{Fe}_{3-x}\text{Ga}_x\text{O}_4$  NPs, the biomedical potential of the samples will be discussed next.

**3.4.1. Viability of  $\text{Fe}_{3-x}\text{Ga}_x\text{O}_4$ @PMAO formulations on cells.** Some of the samples,  $\text{Fe}_{2.86}\text{Ga}_{0.14}\text{O}_4$ ,  $\text{Fe}_{2.73}\text{Ga}_{0.27}\text{O}_4$  and  $\text{Fe}_{2.42}\text{Ga}_{0.57}\text{O}_4$ , were functionalized with poly(maleic anhydride alt-1-octadecene) (PMAO) polymer in order to stabilize in water solution. The handicap of this kind of recovering is the difficulty in obtaining individual particles with polymer coatings as the particles usually agglomerate. Nevertheless, hydrodynamic sizes were measured with dynamic light scattering and values of 15(2), 27(3) and 126(23) nm for the  $\text{Fe}_{2.86}\text{Ga}_{0.14}\text{O}_4$ @PMAO,  $\text{Fe}_{2.73}\text{Ga}_{0.27}\text{O}_4$ @PMAO and  $\text{Fe}_{2.42}\text{Ga}_{0.57}\text{O}_4$ @PMAO respectively, were obtained, indicating a low degree of aggregation for nanoparticles with less gallium content (Fig. S5 in the ESI†). At the same time, the zeta potentials obtained for these preparations ( $-39.0$  (4.9),  $-40.7$  (5.9) and  $-41.8$  (8.3) mV) are indicative of the stability of the sample colloids. Nonetheless, in the case of  $\text{Fe}_{2.42}\text{Ga}_{0.57}\text{O}_4$ @PMAO, the PMAO coating has not been very effective as sizes bigger than those observed by TEM or DRX are observed, being evident in the clusterization of the nanoparticles and the formation of agglomerates.

The cytotoxicity study presented in Fig. 8 aims to analyze if  $\text{Fe}_{3-x}\text{Ga}_x\text{O}_4$  NPs with a significant amount of Ga can impair the viability of cells. For this study, the  $\text{Fe}_{2.42}\text{Ga}_{0.57}\text{O}_4$ @PMAO sample was selected because it presents a substantial content of gallium while still keeping a fair magnetic moment for biomedical applications. The study was carried out at several time points every 24 h until 96 h and at two different concentrations ( $C_1 = 0.01 \mu\text{g}_{\text{NP}}$  per cell and  $C_2 = 0.1 \mu\text{g}_{\text{NP}}$  per cell). Fig. 8 shows that cells incubated with sample  $\text{Fe}_{2.42}\text{Ga}_{0.57}\text{O}_4$ @PMAO grow at the same rate as the control (cells without NPs, blue bars), with no significant differences between the two concentrations ( $C_1$  and  $C_2$ ). Therefore, it can be concluded that  $\text{Fe}_{3-x}\text{Ga}_x\text{O}_4$ @PMAO formulations with  $x \leq 0.57$  are not toxic for cells in the 0.01–0.1  $\mu\text{g}_{\text{NP}}$  per cell concentration range.

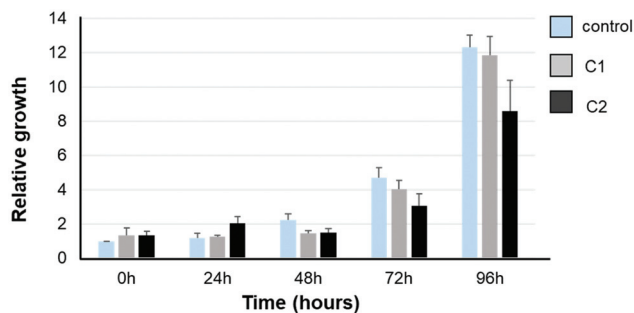


Fig. 8 Viability assay of cells incubated with sample  $\text{Fe}_{2.42}\text{Ga}_{0.57}\text{O}_4$ @PMAO using 2 different concentrations of NPs ( $C_1 = 0.01 \mu\text{g}_{\text{NP}}$  per cell and  $C_2 = 0.1 \mu\text{g}_{\text{NP}}$  per cell) at different time points (from 0 to 96 h). Growth rates were plotted as relative increase compared to 0 h. Values are represented as the mean and standard error of 3 independent experiments.

**3.4.2. Relaxivity measurements of  $\text{Fe}_{3-x}\text{Ga}_x\text{O}_4$ .** The ability of a magnetic agent to modify relaxation times ( $T_1$  and  $T_2$ ) is described by the longitudinal ( $r_1$ ) and transversal relaxivity values ( $r_2$ ), calculated from the slope in the plot of the concentration of the contrast agent *versus* the corresponding  $1/T_1$  and  $1/T_2$ . In general,  $T_1$  relaxation of water protons is related to the regime of the inner sphere of paramagnetic centers where the chemical exchange of protons occurs, and relaxation  $T_2$  is attributed to the regime of the external sphere where the diffusion of the protons through the magnetic particle is dominant.<sup>63</sup> Synthesized magnetite nanoparticles with not very low sizes and superparamagnetic behaviour are expected to behave as  $T_2$  contrast agents.<sup>64</sup> Considering that relaxation strongly depends on the saturation magnetization of the nanoparticles, because of the induction of more effective magnetic relaxations to the water protons, the compositions with the highest values of magnetic saturation have been selected to perform relaxivity studies.

In this way, the longitudinal ( $T_1$ ) and transverse ( $T_2$ ) relaxation times were measured for water soluble PMAO functionalized  $\text{Fe}_{2.86}\text{Ga}_{0.14}\text{O}_4$ @PMAO,  $\text{Fe}_{2.73}\text{Ga}_{0.27}\text{O}_4$ @PMAO and  $\text{Fe}_{2.42}\text{Ga}_{0.57}\text{O}_4$ @PMAO nanoparticles in different concentrations (0.33, 0.25, 0.2, 0.1 and 0.05 mM) in distilled water at 37 °C under a field of 1.4 T, which are shown in Fig. 9. The relaxivities ( $r_1$  and  $r_2$ ) obtained along with the  $r_2/r_1$  ratios are shown in Table 3.

All the analysed samples have shown considerable high  $r_1$  and  $r_2$  values, which are above the relaxivities observed for commercial contrast agents (commercial AMI-227, SHU-555C ( $r_1 = 2.9 \text{ mM}^{-1} \text{ s}^{-1}$ ,  $r_2 = 69 \text{ mM}^{-1} \text{ s}^{-1}$ ) or for gallium ferrite nanoparticles or other synthesized magnetite nanoparticles of similar sizes.<sup>22</sup> Contrast agents are usually classified according to their relationship of relaxation; therefore, if materials show a high  $r_2/r_1$  ratio they are classified as  $T_2$  contrast agents, enhancing the dark contrast and when the  $r_1$  values are high and the  $r_2/r_1$  ratio is close to 1,  $T_1$  contrast agents are obtained.<sup>65</sup> In our case, different relaxation values were

**Table 3** Experimental relaxivity values obtained at 1.4 T for the  $\text{Fe}_{2.86}\text{Ga}_{0.14}\text{O}_4$ @PMAO,  $\text{Fe}_{2.73}\text{Ga}_{0.27}\text{O}_4$ @PMAO and  $\text{Fe}_{2.42}\text{Ga}_{0.57}\text{O}_4$ @PMAO samples

Sample	$r_1$ ( $\text{mM}^{-1}\text{s}^{-1}$ )	$r_2$ ( $\text{mM}^{-1}\text{s}^{-1}$ )	$r_2/r_1$
$\text{Fe}_{2.86}\text{Ga}_{0.14}\text{O}_4$ @PMAO	51	532	10.4
$\text{Fe}_{2.73}\text{Ga}_{0.27}\text{O}_4$ @PMAO	15	131	8.7
$\text{Fe}_{2.42}\text{Ga}_{0.57}\text{O}_4$ @PMAO	11	635	55

obtained depending on the gallium content. Two of the samples present  $r_2/r_1$  ratios larger than 10 ( $\text{Fe}_{2.86}\text{Ga}_{0.14}\text{O}_4$ @PMAO and  $\text{Fe}_{2.42}\text{Ga}_{0.57}\text{O}_4$ @PMAO), and they were considered dark contrast agents. Considering that  $r_2$  values are quite dependent on magnetization, degree of crystallinity, size and aggregation of the nanoparticles, the high value of magnetization at R.T ( $85(1) \text{ Am}^2 \text{ kg}^{-1}$ ) for  $\text{Fe}_{2.86}\text{Ga}_{0.14}\text{O}_4$ @PMAO and the tendency to agglomeration for  $\text{Fe}_{2.42}\text{Ga}_{0.57}\text{O}_4$ @PMAO nanoparticles in aqueous solution (126 (23) nm) may explain the high  $r_2$  values obtained.<sup>66</sup> Ferrite NPs have been exhaustively studied as contrast agents due to their versatility to tune their magnetic response. Nickel doped iron oxides with core-shell structures were prepared and relaxivities  $r_1$  and  $r_2$  comparable with commercial chelated contrasts were obtained.<sup>67</sup> Nevertheless the research is mainly focused on manganese and zinc substituted iron oxides due to the low cytotoxicity of these materials. In J. A. Peters' review Mn-Zn ferrites with different sizes, magnetization, coating and morphologies were studied and only in the case of  $\text{Mn}_x\text{Fe}_{0.3-x}\text{O}_4$  NPs with sizes above 18 nm and maximum magnetization ( $90 \text{ emu g}^{-1}$ ) present transversal relaxivities above  $700 \text{ mM}^{-1}\text{s}^{-1}$ .<sup>14,66</sup> In our case, the biocompatible  $\text{Fe}_{2.86}\text{Ga}_{0.14}\text{O}_4$ @PMAO sample with a smaller size and smaller amount of doping cation reaches a value of  $r_2 = 532 \text{ mM}^{-1}\text{s}^{-1}$  (at 1.5 T), mainly due to a proper control of the synthetic method which yields very crystalline and homogeneous particles. More scarce is the result concerning the development of substituted ferrites to enhance longitudinal relaxivity. Recently, controlling the doping amount of

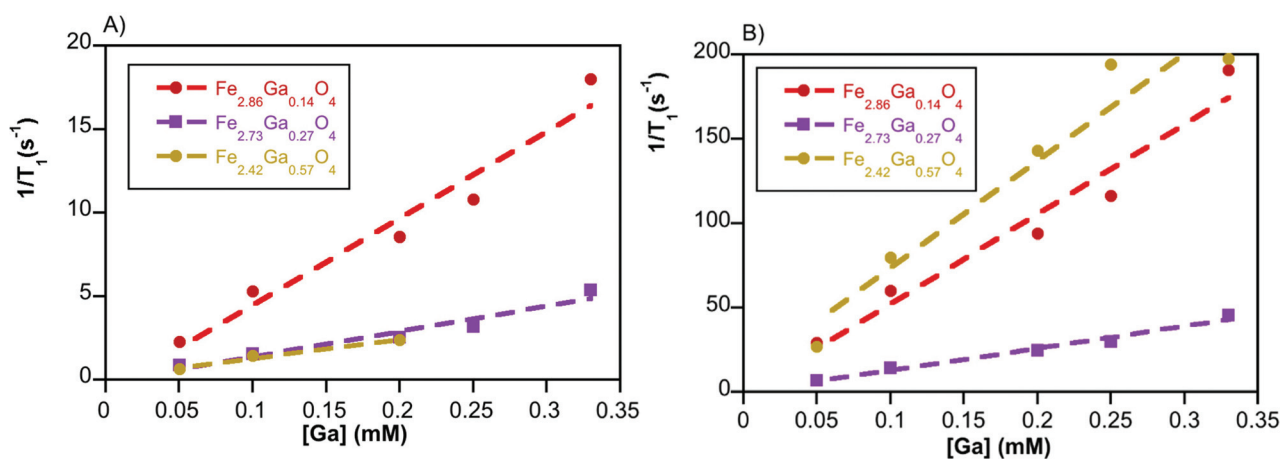


**Fig. 9** Ga concentration dependent longitudinal (A) and transversal (B) relaxivity curves of  $\text{Fe}_{2.86}\text{Ga}_{0.14}\text{O}_4$ @PMAO,  $\text{Fe}_{2.73}\text{Ga}_{0.27}\text{O}_4$ @PMAO and  $\text{Fe}_{2.42}\text{Ga}_{0.57}\text{O}_4$ @PMAO samples.

copper (4% mol) in  $\text{Fe}_3\text{O}_4$  by means of microwave synthesis, relaxivities  $r_1 = 15.7 \text{ mM}^{-1}\text{s}^{-1}$  (at 1.5 T) and  $r_2/r_1 = 2.1$  were obtained. The authors claim that the thin coating recovering the magnetic nuclei also contributes to enhance the longitudinal relaxivity.<sup>68</sup> For the  $\text{Fe}_{2.73}\text{Ga}_{0.27}\text{O}_4@\text{PMAO}$  sample, similar relaxivities have been observed ( $r_1$  and  $r_2$  values, 15 and  $131 \text{ mM}^{-1}\text{s}^{-1}$ , respectively;  $r_2/r_1 = 8.7$ ), also related with an adequate coating. These values are also similar to those observed for manganese substituted ferrites,<sup>69</sup> which opens up the way for research and improvement of these materials as dual mode  $T_1/T_2$  contrast agents. Taking into account the characteristics of the nanoparticles, decreasing saturation magnetization, variable sizes and aggregation in solution, different surface/volume relationships and different amounts of paramagnetic cations on the surface, which condition the temporary binding or the diffusion of the water protons on the nanoparticles, it is difficult to provide an accurate explanation for the enhanced relaxation  $T_1$  and  $T_2$  in this system.<sup>70</sup> Based on the results obtained, further studies should be carried out in order to better control the synthesis route and coating process and thus decipher the exact position of gallium in the structure and its impact on the magnetic response of the system. However, the results presented here are highly promising, encouraging further study of the role of gallium as a dopant in ferrites.

## Conclusions

We have provided the successful preparation of gallium-doped ferrites  $\text{Fe}_{3-x}\text{Ga}_x\text{O}_4$  in the  $0.14 < x < 1.35$  range from thermal decomposition of metallo-organic precursors, the sizes in all the cases being lower than 10 nm. Gallium doping has not only been proved by X-ray diffraction techniques but XANES measurements have also corroborated the  $\text{Ga}^{3+}$  incorporation in the spinel lattice; in particular,  $\text{Ga}^{3+}$  and  $\text{Fe}^{3+}$  ions occupy both tetrahedral and octahedral sites. Nevertheless, the relationship between tetrahedral/octahedral gallium is not maintained constant but changes with the gallium content in the samples, which clearly conditions the magnetic response of the nanoparticles. Compositions with a moderate content of  $\text{Ga}^{3+}$  (5% or 10%,  $0.14 \leq x \leq 0.27$ ) are more suitable to maximize the saturation magnetization in the  $\text{Fe}_{3-x}\text{Ga}_x\text{O}_4$  NP family. Specifically, the sample  $\text{Fe}_{2.86}\text{Ga}_{0.14}\text{O}_4$  presents an  $M_s$  of  $110 \text{ Am}^2 \text{ kg}^{-1}$  at low temperature, which is above magnetite's saturation magnetization. The biocompatibility of water-soluble colloids of PMAO coated  $\text{Fe}_{3-x}\text{Ga}_x\text{O}_4@\text{PMAO}$  NPs offer the opportunity to address the application of this kind of material in 'in vivo' biological processes. In fact, some of the compositions ( $\text{Fe}_{2.86}\text{Ga}_{0.14}\text{O}_4@\text{PMAO}$  and  $\text{Fe}_{2.42}\text{Ga}_{0.57}\text{O}_4@\text{PMAO}$ ) perform as enhanced negative contrast agents in MRI, and the  $\text{Fe}_{2.73}\text{Ga}_{0.27}\text{O}_4@\text{PMAO}$  system with an intermediate ratio of relaxation  $r_2/r_1 \sim 8.7$  behaves as a  $T_1$  and  $T_2$  dual contrast agent. The present work has revealed that the proper tailoring of the size of the nanoparticles, under 10 nm, together with a controlled amount of  $\text{Ga}^{3+}$  yield very promising magnetic biomaterials to be applied as enhanced-contrast agents.

## Conflicts of interest

The authors declare no conflict of interest.

## Acknowledgements

This work was partially supported by institutional funding from the Ministry of Economy and Competitiveness and Basque Government under Projects MAT2019-106845RB-100 (AEI/FEDER, UE), and GU\_IT1226-19. Dr I. Castellanos-Rubio thanks the Horizon 2020 Program for the financial support provided through a Marie Skłodowska-Curie fellowship (798830). L. M. acknowledges the financial support provided through a postdoctoral fellowship from the Basque Government (POS-2019-2-0017). The authors thank the technical and personnel support provided by SGIker (UPV/EHU/ERDF, EU). We thank Elettra (XAFS beamline) for the allocation of the synchrotron radiation beamtime and the funding for travel support for M. I. under the project CALIPSOplus. We also thank D. Oliveira de Souza for his assistance and help in XAFS beamline.

## References

- 1 D. Liu, J. Li, C. Wang, L. An, J. Lin, Q. Tian and S. Yang, *Nanomed. Nanotechnol.*, 2020, **32**, 102335.
- 2 X. Qi, L. Xiong, J. Peng and D. Tang, *RSC Adv.*, 2017, **7**(32), 19604–19610.
- 3 J. Mohapatra, F. Zeng, K. Elkins, M. Xing, M. Ghimire, S. Yoon, S. R. Mishra and J. P. Liu, *Phys. Chem. Chem. Phys.*, 2018, **20**(18), 12879–12887.
- 4 S. Wu, L. Gu, J. Qin, L. Zhang, F. Sun, Z. Liu, Y. Wang and D. Shi, *ACS Appl. Mater. Interfaces*, 2020, **12**(4), 4193–4203.
- 5 D. Li, M. Deng, Z. Yu, W. Liu, G. Zhou, W. Li, X. Wang, D. P. Yang and W. Zhang, *ACS Biomater. Sci. Eng.*, 2018, **4**(6), 2143–2154.
- 6 C. Pereira, A. M. Pereira, C. Fernandes, M. Rocha, R. Mendes, M. P. Fernández-García, A. Guedes, P. B. Tavares, J. M. Grenèche, J. P. Araújo and C. Freire, *Chem. Mater.*, 2012, **24**(8), 1496–1504.
- 7 N. D. Thorat, R. A. Bohara, H. M. Yadav and S. A. Tofail, *RSC Adv.*, 2016, **6**(97), 94967–94975.
- 8 M. Soleymani, S. Khalighfard, S. Khodayari, H. Khodayari, M. R. Kalhori, M. R. Hadjighassem, Z. Shaterabadi and A. M. Alizadeh, *Sci. Rep.*, 2020, **10**(1), 1–14.
- 9 R. A. Revia and M. Zhang, *Mater. Today*, 2015, **19**, 157–168.
- 10 B. H. Kim, N. Lee, H. Kim, K. An, Y. I. Park, Y. Choi, K. Shin, Y. Lee, S. G. Kwon, H. B. Na, J. G. Park, T. Y. Ahn, Y. W. Kim, W. K. Moon, S. H. Choi and T. Hyeon, *J. Am. Chem. Soc.*, 2011, **133**(32), 12624–12631.
- 11 Z. Zhou, L. Wang, X. Chi, J. Bao, L. Yang, W. Zhao, Z. Chen, X. Wang, X. Chen and J. Gao, *ACS Nano*, 2013, **7**(4), 3287–3296.

- 12 B. Lin, X. Wu, H. Zhao, Y. Tian, J. Han, J. Liu and S. Han, *Chem. Sci.*, 2016, **7**(6), 3737–3741.
- 13 Z. Zhao, C. Sun, J. Bao, L. Yang, R. Wei, J. Cheng, L. Hongyu and J. Gao, *J. Mater. Chem. B*, 2018, **6**(3), 401–413.
- 14 L. Yang, L. Ma, J. Xin, A. Li, C. Sun, R. Wei, Z. Chen, H. Lin and J. Gao, *Chem. Mater.*, 2017, **29**, 3038–3047.
- 15 L. Yang, Z. Zhou, H. Liu, C. Wu, H. Zhang, G. Huang, H. Ai and J. Gao, *Nanoscale*, 2015, **7**(15), 6843–6850.
- 16 M. Colombo, S. Carregal-Romero, M. F. Casula, L. Gutiérrez, M. P. Morales, I. B. Böhm, J. Heverhagen, D. Prospero and J. W. Parak, *Chem. Soc. Rev.*, 2012, **41**(11), 4306–4334.
- 17 E. Mazarío, J. Sánchez-Marcos, N. Menéndez, M. Cañete, A. Mayoral, S. Rivera-Fernández, J. M. de la Funete and P. Herrasti, *J. Phys. Chem. C*, 2015, **119**(12), 6828–6834.
- 18 R. Madru, T. A. Tran, J. Axelsson, C. Ingvar, A. Bibic, F. Ståhlberg, L. Knutsson and S. E. Strand, *Am. J. Nucl. Med. Mol. Imaging*, 2014, **4**(1), 60–69.
- 19 A. Lahooti, S. Sarkar, H. S. Rad, A. Gholami, S. Nosrati, R. N. Muller, S. Laurent, C. Grüttner, P. Geramifar, H. Yousefnia, M. Mazidi and M. Mazidi, *J. Radioanal. Nucl. Chem.*, 2017, **311**(1), 769–774.
- 20 J. Pellico, A. V. Lechuga-Vieco, E. Almarza, A. Hidalgo, C. Mesa-Nuñez, I. Fernández-Barahona, J. A. Quintana, J. Bueren, J. A. Enríquez, J. Ruiz-Cabello and F. Herranz, *Sci. Rep.*, 2017, **7**, 13242.
- 21 M. Evertsson, P. Kjellman, M. Cinthio, R. Andersson, T. A. Tran, G. Grafström, H. Toftvall, S. Fredriksson, C. Ingvar, S. E. Strand and T. Jansson, *Sci. Rep.*, 2017, **7**(1), 1–9.
- 22 C. C. Huang, C. H. Su, M. Y. Liao and C. S. Yeh, *Phys. Chem. Chem. Phys.*, 2009, **11**(30), 6331–6334.
- 23 J. Sánchez, D. A. Cortés-Hernández, J. C. Escobedo-Bocardo, R. A. Jasso-Terán and A. Zugasti-Cruz, *J. Mater. Sci. Mater. Med.*, 2014, **25**(10), 2237–2242.
- 24 R. P. Warrell Jr., *Cancer Am. Cancer Soc.*, 1997, **80**, 1680–1685.
- 25 É. A. Enyedy, O. Dömötör, E. Varga, T. Kiss, R. Trondl, C. G. Hartinger and B. K. Keppler, *J. Inorg. Biochem.*, 2012, **117**, 189–197.
- 26 H. Gamari-Seale and P. A. Papamantellos, *Phys. Status Solidi B*, 1968, **29**(1), 323–331.
- 27 J. Ghose, G. C. Hallam and D. A. Read, *J. Phys. C: Solid State Phys.*, 1997, **10**(7), 1051.
- 28 V. L. Pool, M. T. Klem, C. L. Chorney, E. A. Arenholz and Y. U. Idzerda, *J. Appl. Phys.*, 2011, **109**(7), 07B529.
- 29 J. Ghose, *J. Solid State Chem.*, 1989, **79**(2), 189–193.
- 30 I. S. Lyubutin, S. S. Starchikov, N. E. Gervits, C. R. Lin, Y. T. Tseng, K. Y. Shih, J. S. Lee, Y. L. Ogarkovaa and N. Y. Korotkova, *Phys. Chem. Chem. Phys.*, 2016, **18**, 22276–22285.
- 31 C. A. J. Lin, R. A. Sperling, J. K. Li, T. Y. Yang, P. Y. Li, M. Zanella, W. H. Chang and W. J. Parak, *Small*, 2008, **4**(3), 334–341.
- 32 J. Rodríguez-Carvajal, *Phys. Rev. B: Condens. Matter Mater. Phys.*, 1993, **192**(1–2), 55–69.
- 33 B. Ravel and M. Newville, *Phys. Scr., T*, 2005, **T115**, 1007–1010.
- 34 S. Ayyappan, G. Panneerselvam, M. P. Antony and J. Philip, *J. Mater. Chem. Phys.*, 2011, **130**, 1300–1306.
- 35 V. Mameli, A. Musinu, A. Ardu, G. Ennas, D. Peddis, D. Niznansky, C. Sangregorio, C. Innocenti, N. T. K. Thanh and C. Cannas, *Nanoscale*, 2016, **8**, 10124–10137.
- 36 K. P. Naidek, F. Bianconi, T. C. Rizuti da Rocha, D. Zanchet, J. A. Bonacin, M. A. Novak, M. G. F. Vaz and H. Winnischofer, *J. Colloid Interface Sci.*, 2011, **358**(1), 39–46.
- 37 J. H. Huang, H. J. Parab, R. S. Liu, T. C. Lai, M. Hsiao, C. H. Chen, H. S. Sheu, J. M. Chen, D. P. Tsai and Y. K. Hwu, *J. Phys. Chem. C*, 2008, **112**(40), 15684–15690.
- 38 A. L. Patterson, *Phys. Rev.*, 1939, **56**, 978–982.
- 39 J. Sánchez, D. A. Cortés-Hernández, J. C. Escobedo-Bocardo, J. M. Almanza-Robles, P. Y. Reyes-Rodríguez, R. A. Jasso-Terán, P. Bartolo-Pérez and L. E. De-León-Prado, *Ceram. Int.*, 2016, **42**, 13755–13760.
- 40 C. C. Huang, C. H. Su, M. Y. Liao and C. S. Yeh, *Phys. Chem. Chem. Phys.*, 2009, **11**, 6331–6334.
- 41 D. L. Burnett, M. H. Harunsani, R. J. Kashtiban, H. Y. Playford, J. Sloan, A. C. Hannon and R. I. Walton, *J. Solid State Chem.*, 2014, **214**, 30–37.
- 42 C. Moya, X. Batlle and A. Labarta, *Phys. Chem. Chem. Phys.*, 2015, **17**, 27373–27379.
- 43 M. Benfatto and C. Meneghini, *Synchrotron Radiation*, Springer, Berlin, 2015.
- 44 P. Eisenberger and B. Lengeler, *Phys. Rev. B: Condens. Matter Mater. Phys.*, 1980, **22**, 3551.
- 45 M. L. Fdez-Gubieda, A. García-Prieto, J. Alonso and C. Meneghini, *Iron Oxides*, ed. D. Faivre, Wiley-VCH, Weinheim, 2016, **17**, 397–422.
- 46 I. Castellanos-Rubio, O. Arriortua, L. Marcano, I. Rodrigo, D. Iglesias-Rojas, A. Barón, A. Olazagoitia-Garmendia, L. Olivi, F. Plazaola, M. L. Fdez-Gubieda, A. Castellanos-Rubio, J. S. Garitaonandia, I. Orue and M. Insausti, *Chem. Mater.*, 2021, **33**(9), 3139–3154.
- 47 M. Wilke, F. Farges, P. E. Petit, G. E. Brown Jr. and F. Martin, *Am. Mineral.*, 2001, **86**(5–6), 714–730.
- 48 J. Chaboy and S. Quartieri, *Phys. Rev. B: Condens. Matter Mater. Phys.*, 1995, **52**(9), 6349–6357.
- 49 D. Alba Venero, L. Fernandez Barquín, J. Alonso, M. L. Fdez-Gubieda, L. Rodríguez Fernández, R. Boada and J. Chaboy, *J. Condens. Matter Phys.*, 2013, **25**(27), 276001.
- 50 I. Castellanos-Rubio, I. Rodrigo, R. Munshi, O. Arriortua, J. S. Garitaonandia, A. Martínez-Amesti, F. Plazaola, I. Orue, A. Pralle and M. Insausti, *Nanoscale*, 2019, **11**, 16635–16649.
- 51 C. Prieto, T. Blasco, M. Cambor and J. Pérez-Parient, *J. Mater. Chem.*, 2000, **10**, 1383–1387.
- 52 F. Porcaro, C. Bonchi, A. Ugolini, E. Frangipani, G. Polzonetti, P. Visca, C. Meneghini and C. Battocchio, *Dalton Trans.*, 2017, **46**, 7082–7091.
- 53 N. Modaresi, R. Afzalzadeh, B. Aslibeiki, P. Kameli, A. G. Varzaneh, I. Orue and V. A. Chernenko, *J. Magn. Magn. Mater.*, 2019, **482**, 206–218.

- 54 L. Guo, X. Shen, X. Meng and Y. Feng, *J. Alloys Compd.*, 2010, **490**, 301–306.
- 55 J. M. D. Coey, *Phys. Rev. Lett.*, 1971, **27**, 1140.
- 56 X. Lasheras, M. Insausti, J. Martínez de la Fuente, I. Gil de Muro, I. Castellanos-Rubio, L. Marcano, M. L. Fernández-Gubieda, A. Serrano, R. Martín-Rodríguez, E. Garaio, J. A. García and L. Lezama, *Dalton Trans.*, 2019, **48**, 11480–11491.
- 57 J. L. Dormann and D. Fiorani, *Magnetic Properties of Fine Particles*, Elsevier, Amsterdam, 1992.
- 58 I. J. Bruvera, P. Mendoza Zélis, M. Pilar Calatayud, G. F. Goya and F. H. Sánchez, *J. Appl. Phys.*, 2015, **118**(18), 184304.
- 59 N. A. Usov, *J. Appl. Phys.*, 2011, **109**, 023913.
- 60 I. Castellanos-Rubio, M. Insausti, E. Garaio, I. Gil de Muro, F. Plazaola, T. Rojo and L. Lezama, *Nanoscale*, 2014, **6**, 7542–7552.
- 61 E. C. Stoner and E. P. Wohlfarth, *Philos. Trans. R. Soc., A*, 1948, **240**, 599–642.
- 62 F. Gazeau, J. Bacri, F. Gendron, R. Perzynski, Y. Raikher, V. Stepanov and E. Dubois, *J. Magn. Magn. Mater.*, 1998, **186**, 175–187.
- 63 A. J. Villaraza, A. Bumb and M. W. Brechbiel, *Chem. Rev.*, 2010, **110**, 2921.
- 64 N. J. J. Johnson, W. Oakden, G. J. Stanisz, R. Scott Prosser and F. C. J. M. van Veggel, *Chem. Mater.*, 2011, **23**, 3714–3722.
- 65 N. Guldris, B. Argibay, Y. V. Kolen'ko, E. Carbó-Argibay, T. Sobrino, F. Campos, L. M. Salonen, M. Bañobre-López, J. Castillo and J. Rivas, *J. Colloid Interface Sci.*, 2016, **472**, 229–236.
- 66 J. A. Peters, *Progress in Nuclear Magnetic Resonance Spectroscopy*, 2020, 120–121, 72–94.
- 67 M. D. Schultz, S. Calvin, P. P. Fatouros, S. A. Morrison and E. E. Carpenter, *J. Mag. Magn. Mat.*, 2007, **311**, 464–468.
- 68 I. Fernández-Barahona, L. Gutiérrez, S. Veintemillas-Verdaguer, J. Pellico, M. P. Morales, M. Catala, M. A. Del Pozo, J. Ruiz-Cabello and F. Herranz, *ACS Omega*, 2019, **4**, 2719–2727.
- 69 G. Huang, H. Li, J. Chen, Z. Zhao, L. Yang, X. Chi, Z. Chen, X. Wang and J. Gao, *Nanoscale*, 2014, **6**, 10404.
- 70 S. Sánchez-Cabezas, R. Montes-Robles, J. Gallo, F. Sancenón and R. Martínez-Mañez, *Dalton Trans.*, 2019, **48**, 3883–3892.